Chemical Engineering Journal 457 (2023) 141176

Contents lists available at ScienceDirect

Chemical Engineering Journal

journal homepage: www.elsevier.com/locate/cej

Electrospun nanofibers of chitosan/polyvinyl alcohol/UiO-66/nanodiamond: Versatile adsorbents for wastewater remediation and organic dye removal

Farhad Ahmadijokani [a,b,c], Hossein Molavi [d], Addie Bahi [b], Stefan Wuttke [e,f], Milad Kamkar [c,g], Orlando J. Rojas [c,h,*], Frank Ko [b,*], Mohammad Arjmand [a,*]

[a] Nanomaterials and Polymer Nanocomposites Laboratory, School of Engineering, University of British Columbia, Kelowna, British Columbia V1V 1V7, Canada
[b] Department of Materials Engineering, University of British Columbia, Vancouver, BC V6T 1Z4, Canada
[c] Bioproducts Institute, Department of Chemical and Biological Engineering, Department of Chemistry and Department of Wood Science, University of British Columbia, 2360 East Mall, Vancouver V6T 1Z3, BC, Canada
[d] Department of Chemistry, Institute for Advanced Studies in Basic Science (IASBS), Gava Zang, Zanjan 45137-66731, Iran
[e] BCMaterials (Basque Centre for Materials, Applications & Nanostructures), Bld. Martina Casiano, 3rd. Floor UPV/EHU Science Park Barrio Sarriena s/n, 48940 Leioa, Spain
[f] IKERBASQUE, Basque Foundation for Science, 48013 Bilbao, Spain
[g] Department of Chemical Engineering, University of Waterloo, 200 University Avenue West, Waterloo, Ontario N2L 3G1, Canada
[h] Department of Bioproducts and Biosystems, School of Chemical Engineering, Aalto University, Vuorimiehentie 1, FI-00076, Espoo, Finland

ARTICLE INFO

Keywords:
Dye removal
Electrospun nanofibers
UiO-66
Nanodiamond
Hybrid nanostructures

ABSTRACT

The appeal of metal–organic frameworks (MOFs) in wastewater treatment is tempered by their polycrystalline, powdery state, and challenges associated with their deployment. In the case of UiO-66, one of the most stable and widely-used MOFs, a low tendency for removing some organic contaminants has been observed on top of the mentioned issues. To address these challenges, herein, we take two complementary steps, i.e., hybridization of UiO-66 with organic nanodiamond (ND) followed by the integration of the hybrid nanoparticles in electrospun polymeric nanofibers based on chitosan/polyvinyl alcohol (PVA). We present the electrospinning of polymer/MOFs as a promising technique to fabricate highly efficient adsorbents for water remediation. We use the electrospun chitosan/PVA nanofibers (ECPN) as a versatile host for MOF nanoparticles that remove cationic methylene blue and anionic Congo red dyes. Four nanofiber composites containing thermally oxidized nanodiamond (TOND), ND, UiO-66, and TOND@UiO-66 are utilized to unravel the effect of nanoparticles type and loading on dye adsorption capacity. It is shown that incorporation of a small loading of nanoparticles in ECPN significantly enhaces the maximum dye adsorption capacity. More importantly, the rationally engineered hybrid TOND@UiO-66 nanoparticles exhibit the best performance in dye adsorption; for instance, an 80 % increase in maximum dye adsorption capacity, from 769 to 1429 mg/g, is recorded for ECPN loaded with TOND@UiO-66 compared to the unfilled ECPN. On top of that, the designed adsorbent showed appreciable regeneration ability after 6 adsorption–desorption cycles. All in all, this study offers a new generation of engineered advanced materials to remove emerging contaminants from water streams.

1. Introduction

Crystalline metal–organic framework (MOF) materials with high surface area, abundant functionalities, tunable pore size, and high affinity to specific molecules have shown great potential for removing water contaminants, such as heavy metal ions, organic drugs, etc. [1–9]. While considerable efforts have been devoted to scale-up, chemistry, and application of MOFs at the lab scale level [10,11], exploratory initiatives must be taken to transcend MOFs into practical wastewater treatment. Processability issues and control of MOF superstructure have become critical rate-limiting steps, hindering real-world applications of MOFs [12–14], especially their prospective use for wastewater

* Corresponding authors.
E-mail addresses: orlando.rojas@ubc.ca, orlando.rojas@aalto.fi (O.J. Rojas), frank.ko@ubc.ca (F. Ko), mohammad.arjmand@ubc.ca (M. Arjmand).

https://doi.org/10.1016/j.cej.2022.141176
Received 22 October 2022; Received in revised form 21 December 2022; Accepted 24 December 2022
Available online 30 December 2022

treatment. Shaping MOFs into macrostructures by accommodating them into electrospun nanofibers is deemed a game-changer approach in order to bring powdery MOFs closer to the industrial applications level [15].

Nanofabrication via electrospinning has had a tremendous impact over the past three decades due to its versatility, simplicity, and affordability [16]. Notably, numerous enterprises have invested in electrospinning technology and thereby have pushed the nanofibers' yearly production capacity to the ton-scale [17]. Placing the atomic-level functional MOF materials into nanofibers with a high surface-to-volume ratio not only can address the processing obstacles but also can retain the MOFs' active sites for interacting with pollutants in aqueous media [15]. For instance, mats comprising ZIF-8/polyvinyl alcohol (PVA) [18] and ZIF-67/polyacrylonitrile (PAN) [19] showed maximum adsorption capacities of 160 and 849 mg/g toward Congo red dye (CR), respectively.

Several approaches can be considered to further improve the design of MOF-based nanocomposites for water remediation, such as the post-modification of MOFs by adding active functional groups, doping, organic ligand modification, and hybridizing with other nanoparticles [3,11,20–23]. Hybridizing MOFs with inorganic nanoparticles, such as graphene oxide (GO) [24], carbon nanotubes (CNTs) [25], nanodiamonds (ND) [26], magnetic nanoparticles [27], covalent organic frameworks (COFs) [28], activated carbon [29], and layered double hydroxide [30] can improve the morphological, stability, kinetic, and physicochemical features for water treatment. For example, the hybrid of ZIF-8 with GO and CNT has shown improved adsorption performance, stability, and reusability for eliminating malachite green (MG) [24]. In another study, Ahmadipouya et al. [27] followed an in situ growth of UiO-66 onto a magnetic Fe_3O_4 core to address separation challenges. They reported high adsorption capacities of 205 and 244 mg/g toward cationic methylene blue (MB) and anionic methyl orange (MO) dyes, respectively.

To design novel MOF hybrids, where the coupling agent is immobilized inside the MOF cages, the existence of binding sites for successful synthesis and anchoring of MOFs is vital. Hence, in the present work, thermally oxidized nanodiamond (TOND) was selected as the substrate to produce MOF-based nanocomposite mainly because of its relatively high surface area, good chemical stability, high affinity toward specific organic dyes, non-toxicity, and numerous surface bridging sites due to the existence of large oxygen-containing functional groups on its surface [31–34]. To unravel the benefits of the hybridization of MOFs with other nanomaterials and electrospinning technology to fabricate nanoparticle-filled nanofiber adsorbents, ND, TOND, UiO-66, and their nanocomposites (TOND@UiO-66) were prepared and incorporated into nanofibers formed with a mixture of chitosan and polyvinyl alcohol (CS/PVA) (Scheme 1). The prepared nanofiber composites were then cross-linked using glutaraldehyde (GA) and tested for cationic MB and anionic CR removal from wastewater. In addition, the systematic adsorbent performance, in terms of adsorption kinetics, isotherms, selectivity, ionic strength, the effect of pH, and reusability, was investigated to verify the applicability of the MOF nanofibers in real wastewater treatment applications.

2. Materials and methods

2.1. Chemicals and instruments

Zirconium chloride ($ZrCl_4$, Sigma-Aldrich), 1,4-benzene dicarboxylic acid (BDC, Sigma-Aldrich), dimethylformamide (DMF, Sigma-Aldrich), ethanol (Sigma-Aldrich), and detonation nanodiamond (ND, NaBond Technologies) were used to synthesize nanoparticles. Chitosan (CS, 75–85 % deacetylated, medium molecular weight, Sigma-Aldrich), polyvinyl alcohol (PVA, molecular weight of 145,000, Sigma-Aldrich), acetic acid (HAc, Sigma-Aldrich), and glutaraldehyde (GA, Sigma-Aldrich) were purchased and used to prepare the electrospun nanofibers. Methylene blue (MB, Sigma-Aldrich) and Congo red (CR, Sigma-Aldrich), sodium hydroxide pellets (NaOH, Sigma-Aldrich), and concentrated hydrochloric acid (HCl, Sigma-Aldrich) were employed to perform the adsorption experiments. FTIR, XRD, BET, TGA, and SEM analysis, detailed in Supplementary Information, were used to explore the structure of the developed materials.

2.2. Synthesis of adsorbent nanoparticles

2.2.1. Preparation of TOND

The oxidation of ND particles was performed to add carboxylic acid groups on their surface, to serve as nuclei sites for UiO-66 growth. Accordingly, 150 mg of ND was heated at 425 °C for 270 min under an air atmosphere [35,36]. The oxidized nanoparticles were stored in a desiccator to prevent moisture adsorption from the air.

2.2.2. Synthesis of TOND@UiO-66 nanocomposite

A 'bottle around ship' (BAS) concept was followed to synthesize TOND@UiO-66 nanocomposite [20,26,37]. Briefly, 60 mg of TOND nanoparticles were dispersed in 20 mL DMF by sonication for 1 h. Thereafter, 530 mg of $ZrCl_4$ was added to the TOND suspension, sonicated for 1 h, and stirred at room temperature for 12 h. Meantime, 380 mg of BDC was dissolved in 20 mL DMF and stirred to prepare a transparent solution. Then, the BDC solution was added to the TOND

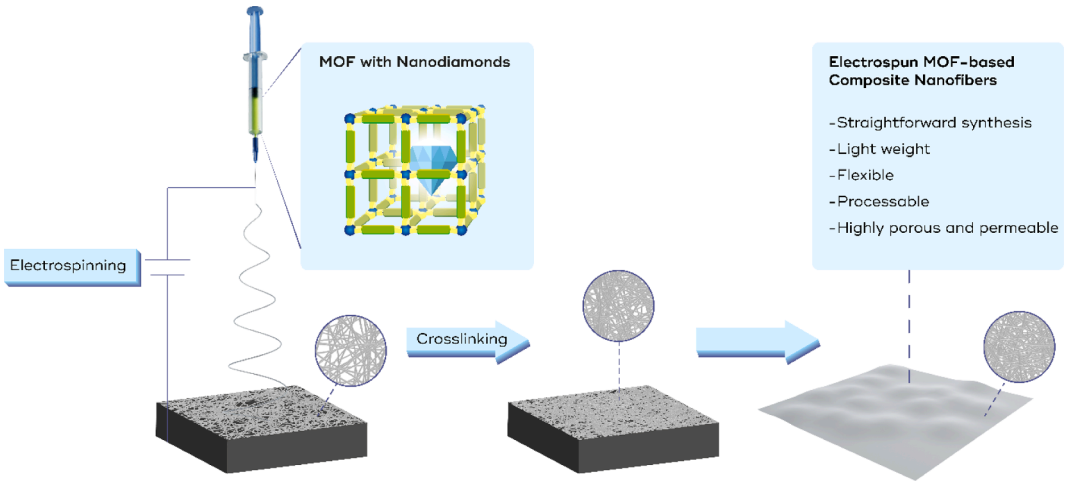

Scheme 1. Schematic illustration of the fabrication of the electrospun TOND@UiO-66 nanofibers.

suspension, sonicated for 1 h, and the mixture was transferred into a Teflon autoclave and heated at 120 °C for 24 h. The prepared gray TOND@UiO-66 nanocomposite was separated by filtration, washed with DMF, and further with ethanol, and then solvent-exchanged by Soxhlet extraction in ethanol for 5 days. Finally, the synthesized nanocomposite was dried at 120 °C under the vacuum for 12 h. The same procedure was used to synthesize pure UiO-66 nanoparticles without adding TOND to the DMF solution [38].

2.3. Preparation of electrospun nanofiber adsorbents

Due to the nature of UiO-66 MOFs, a MOF-first strategy [16] was utilized to prepare nanofiber composites. Accordingly, 7.5 mg of TOND@UiO-66 was mixed with 7.5 mL of distilled water using a bath sonicator for 30 min, followed by stirring at room temperature for 12 h. In the next step, 375 mg of PVA powder was added to the suspension, sonicated for 30 min, and finally stirred at room temperature for 12 h. In the meantime, 125 mg of CS powder was dissolved in 2.5 mL of 2 % v/v HAc solution, and stirring was continued at room temperature for 12 h. In order to prepare a homogeneous suspension for electrospinning, the CS solution was added to the nanoparticle suspensions plus 30 min of sonication and 12 h of stirring at room temperature.

High voltage electrospinning (22–25 kV- syringe tip to collector distance: 15 cm), followed by drying nanofibers (under vacuum for a day) and cross-linking with GA was performed to fabricate the final nanofiber composite for dye removal. To evaluate the performance of the TOND@UiO-66 nanofiber compared to bare UiO-66, ND, and TOND, the same procedure was employed to fabricate their nanofiber composites. The following terminology (Table 1) is used throughout the manuscript for samples with the parent composition of 125 mg CS, 375 mg PVA, 9.8 mL water, and 0.2 mL HAc.

2.4. Dye removal experiments

To conduct the adsorption study, measured amounts of each adsorbent were added to 50 mL of dye solutions (20–500 mg/L) and shaken in a dark place for 180 min at room temperature. Afterward, the concentration of dyes was measured by ultraviolet–visible (UV–Vis) spectroscopy. Finally, the removal percentage, adsorption capacity (q_t) at specific intervals (time t), as well as adsorption capacity (q_e) at equilibrium, were calculated using Eqs. S1-S3, respectively [35]. In order to fully exploit the adsorbents, they were dried at 80 °C for 12 h under a vacuum before the experiments.

3. Results and discussion

3.1. Characterization of adsorbent nanoparticles

3.1.1. FTIR analysis

The surface chemistry of the adsorbents and the interaction of the designed MOF components were studied by FTIR. Fig. 1a displays the FTIR spectra of ND, TOND, UiO-66, and TOND@UiO-66 hybrid. The FTIR spectrum of the as-received ND shows the characteristic absorption peaks at 1000–1200 cm^{-1} (ν(C—O—C)), 1630–1750 cm^{-1} (ν(C═O)), 2850–2950 cm^{-1} (ν(C—H)), and 3250–3650 cm^{-1} (ν(O—H)), in agreement with previous findings [31,39,40]. The increased absorption peaks at 1722 cm^{-1} (ν(C═O) and 1100–1200 cm^{-1} (ν(C—O—C)) were observed in TOND compared to ND, an indicator of carboxylic acid formation from different functional groups [39,41]. The absorption band in the spectrum of UiO-66 at 3200–3700 cm^{-1} belongs to the stretching vibration of O—H bonds of BDC molecules. The adsorbed or inter-crystalline water molecules also appeared in the 3200–3700 cm^{-1} spectrum range [38,42]. The sharp peaks at around 1700 and 1400 cm^{-1} are assigned to the symmetrical stretching vibration of the C═O bonds of BDC molecules.

Two sharp peaks observed at 1502 and 1578 cm^{-1} are attributed to the stretching vibration of C═C bonds of BDC molecules [38]. The observation of these characteristic peaks suggests that the signal associated with UiO-66 nanoparticles originated from the presence of BDC ligands in their structures [42,43]. The peaks at 661 and 765 cm^{-1} come from the asymmetric and symmetric stretching vibration of O–Zr–O bonds, confirming the formation of coordination bonds between Zr^{4+} ions as the coordination center and the BDC molecules as the bridging ligands [44,45]. The emergence of characteristic peaks of ND and UiO-66 in the spectrum of TOND@UiO-66 confirms the successful synthesis of the nanocomposite. It should be noted that the absorption peak position belonging to the stretching vibration of C═O bonds slightly shifted to lower wavenumbers in TOND@UiO-66, mainly due to the coordination of the Zr center of UiO-66 with the carboxylic acid functional groups of TOND. [26]. A similar observation was reported by Han et al. [46] in the case of the MIL-68 MOF and CNT (CNT@MIL-68) nanocomposites.

Table 1
Electrospun chitosan-polyvinyl alcohol nanofibers with 1.5 wt% of different nanoparticle additives.

Specimens	Nanoparticles
ECPN	–
ECPN/N	ND
ECPN/T	TOND
ECPN/U	UiO-66

3.1.2. XRD analysis

XRD patterns of the synthesized adsorbent nanoparticles were obtained and shown in Fig. 1b to study the crystallinity of the parent materials and their nanocomposites. The XRD patterns of ND unfold the presence of all the characteristic diffraction peaks of ND (2θ = 16.2°, 21.4°, and 43.5°), consistent with previous reports [31,47]. TOND demonstrated similar XRD patterns to ND with minor peak position and intensity changes. Accordingly, the peak at 2θ = 21.4°, related to a graphite-type lattice, slightly shifted to lower degrees and its intensity decreased after thermal oxidation, confirming the reduction of graphite layer number on the surface of ND particles. Three sharp diffraction peaks at 2θ = 7.3°, 8.5°, and 25.8° in the XRD patterns of UiO-66 and TOND@UiO-66 belong to the (1 1 1), (2 0 0), and (6 0 0) crystal planes, respectively [43]. The good agreement of the XRD patterns with simulated UiO-66 and the literature confirms the successful synthesis of UiO-66 specimens in our study [38,42,43]. The XRD observation revealed that the presence of TOND in TOND@UiO-66 did not interrupt the formation of the UiO-66 crystalline structure.

3.1.3. N_2 adsorption–desorption analysis

N_2 adsorption–desorption isotherms assessed the porosity and texture of nanoparticles at 77 K (Fig. 1c). The isotherms of the TOND are similar to Type IV, demonstrating mesoporous (pore diameter > 2 nm) structures [33]. Pure UiO-66 nanoparticles showed Type I isotherms with a predominantly microporous structure [48]. Fig. 1c demonstrates that the TOND@UiO-66 isotherms are relatively a combination of Type I and Type IV isotherms, showing a sharp increase in N_2 adsorption at sufficiently low relative pressures, continuous growth to high pressures, and hysteresis at high pressures. Moreover, the N_2 gas uptake of TOND@UiO-66 increased continuously with the relative pressure from 0.1 to 0.3, confirming the presence of larger micropores, mainly due to the existence of the TOND in the structure. Table 2 summarizes the pore textural properties of nanoparticles. TOND and UiO-66 nanoparticles have Brunauer-Emmett-Teller (BET) surface areas of 331 and 1050 m^2/g, respectively, which is in line with previous reports for these materials [38,47]. The BET surface area of TOND@UiO-66 experienced a 20 % decrease compared to pure UiO-66, mainly due to the higher density of TOND and its lower porosity. Table 2 shows that the TOND@UiO-66 nanocomposite has a slightly larger pore diameter and pore volume

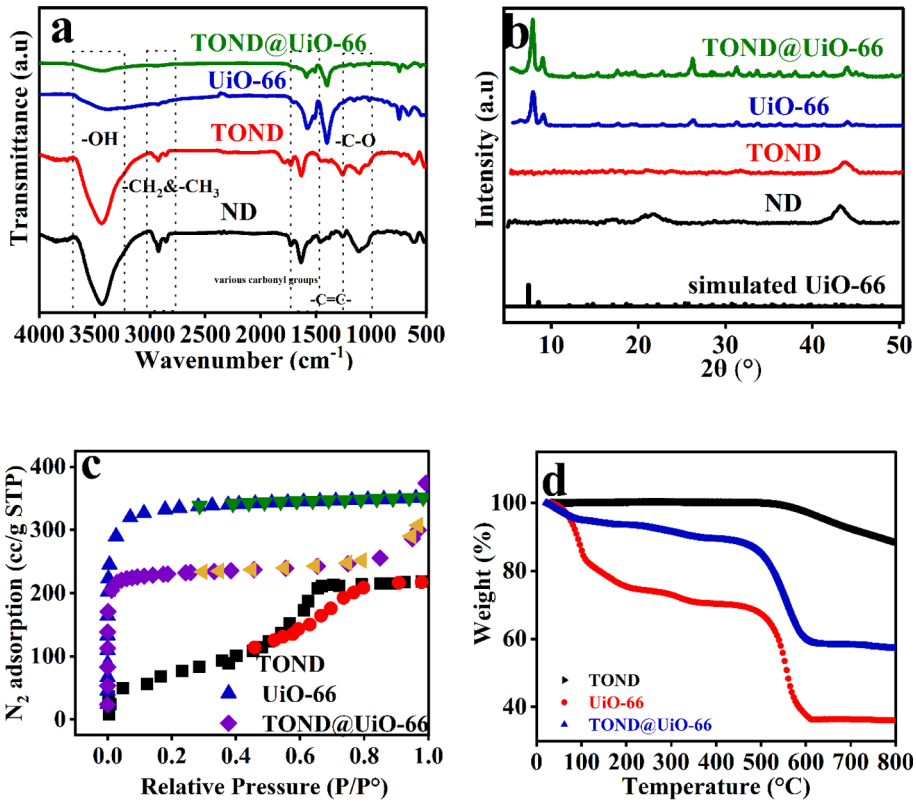

Fig. 1. a) FTIR spectra, b) XRD patterns, c) N_2 adsorption–desorption isotherms, and d) TGA thermograms of nanoparticles.

Table 2
Textural properties of pristine materials and their composite.

Samples	S_{BET} (m^2/g)	Pore volume (cm^3/g)	Average pore diameter (nm)	Zeta potential
ND[a]	291	–	–	−2.61
TOND	331	–	–	−12.48
UiO-66	1050	0.521	2.1	−0.28
TOND@UiO-66	845	0.541	2.5	−3.81

[a] Data reported from Ref. [33].

than pure UiO-66, which may be caused by the formation of new pores between UiO-66 crystals and TOND particles. The larger pores in the structure of TOND@UiO-66 nanocomposite facilitate mass diffusion from bulk to intra-particles, which are beneficial to the adsorption of dye molecules [48].

3.1.4. Thermogravimetric analysis

The thermal stability of nanoparticles and their nanocomposite (TOND@UiO-66) was investigated with thermogravimetric analysis (TGA) and displayed in Fig. 1d. Only a slight reduction in the TOND weight was observed at temperatures higher than 500 °C, which might be attributed to the degradation of various oxygen-containing functional groups on the surface of TOND particles [34,49]. The somewhat higher thermal stability of TOND in comparison with the as-received ND particles may be due to a reduction in the number of graphite layers on the surface of TOND particles, further confirming the conversion of different functional groups on the surface of the ND particles to carboxylic acid groups during thermal oxidation [47,50]. UiO-66 and TOND@UiO-66 showed three weight loss steps by increasing the temperature up to 800 °C. Removing guest water or physically adsorbed water could account for weight loss in the 60–120 °C range [51,52]. The second weight loss in the range of 120–250 °C could be attributed to the removal of solvent molecules. The following weight reduction step for UiO-66 and TOND@UiO-66 was observed at temperatures higher than 490 °C, possibly due to the collapse of their framework [25]. According to our results, pristine UiO-66 and TOND@UiO-66 exhibited similar thermal stabilities, demonstrating that the thermal stability of UiO-66 was not significantly affected by TOND. However, the final ash content of the nanocomposite is more than that of pristine UiO-66, primarily due to the high thermal stability of TOND in the nanocomposite structure.

3.1.5. SEM analysis

The particle size and morphology of the nanoparticles were investigated by SEM images and are displayed in Fig. 2. Accordingly, both pristine and thermally oxidized ND are nearly spherical, with particle sizes smaller than 40 nm. UiO-66 possesses a cubic shape with a particle size smaller than 200 nm, in line with literature reports [47,53,54]. The TOND@UiO-66 morphology is reasonably similar to UiO-66, with minor changes in particle size irregularity. Accordingly, the particle sizes decreased in TOND@UiO-66, and the crystal became more irregular. Coordinating the Zr^{4+} center of the UiO-66 framework with the oxygen-containing functional groups (especially carboxylic acid groups) of TOND inhibits MOF nanocrystal aggregation, thereby enhancing their dispersion [25,53].

3.2. Characterization of electrospun nanofibers

3.2.1. FTIR analysis

FTIR analysis assessed the interfacial interactions between nanoparticles and matrix in the nanofiber composites. Accordingly, as shown in Fig. 3a, cross-linked CS/PVA (ECPN) has the characteristic peaks of CS and PVA. The broad absorption bands in the range of 3150–3600 cm^{-1} could originate from stretching vibration of –OH and –NH groups and the formation of intramolecular or intermolecular hydrogen bonds of –OH groups of PVA [39,55]. CS and PVA showed two absorption bands between 2870 and 2980 cm^{-1}, probably due to their aliphatic

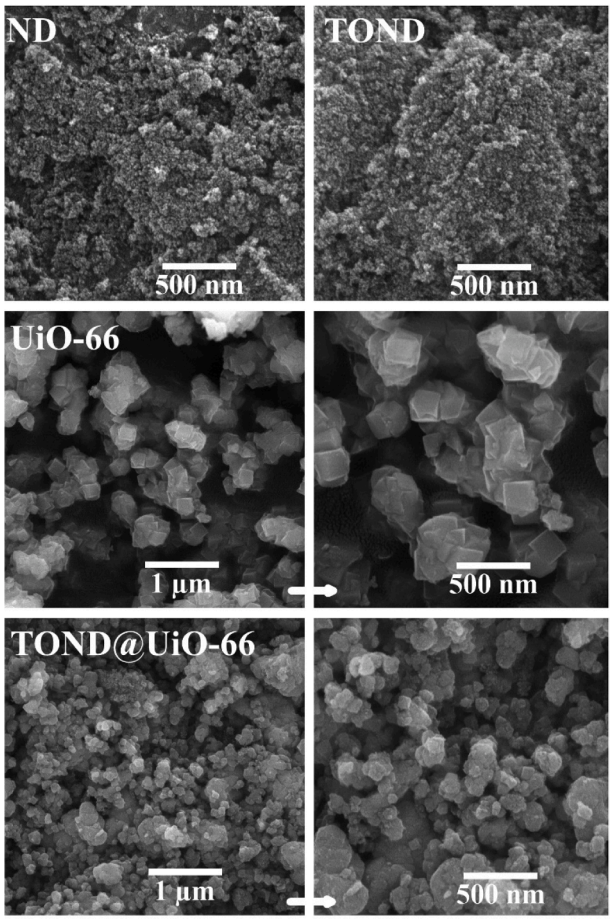

Fig. 2. SEM images of the synthesized nanoparticles.

–C—H stretching vibrations [56]. CS amide groups may be responsible for the strong absorption bands observed in the range of 1500–1650 cm^{-1} [35,39]. The strong absorption band at 1380 cm^{-1} could correspond to the symmetrical deformation mode of –C—H bonds of both CS and PVA. The sharp absorption bands observed in 1000–1100 cm^{-1} could be assigned to the stretching vibration of –C—O bonds in both polymers [57]. Nanofibers composites exhibited all characteristic peaks of their constituents, including polymers and nanoparticles. However, the broad absorption band in the range of 3150–3600 cm^{-1}, related to the stretching vibration of hydrogen-bonded –N—H and –O—H groups, shifts to lower wavenumbers. This red shift confirms the formation of hydrogen bonds between the –N—H and –O—H groups of the polymer matrix and the polar functional groups of nanoparticles [58]. Delavar and Shojaei observed comparable results in their study on thermally oxidized and untreated ND particles [39].

3.2.2. XRD analysis

The possible effects of the incorporated nanoparticles on the crystallinity of nanofibers composed of semicrystalline CS and PVA were investigated using XRD. Fig. 3b displays the XRD patterns of pure CS/PVA nanofibers and nanofiber composites. The cross-linked CS/PVA matrix exhibits a broad diffraction peak in the range of 15-30° due to its amorphous structure, in agreement with the literature [58,59]. Nanocomposite nanofibers containing different nanoparticles show XRD patterns nearly similar to pure nanofibers, indicating that the nanoparticles did not significantly affect the crystalline structure of the CS/PVA matrix. It is worth mentioning that the diffraction patterns of each nanoparticle appeared in the same position as their pure crystals but with decreased peak intensities compared to those of pure nanoparticles. This observation also endorses that the crystalline structure of nanoparticles remains intact under the nanofiber fabrication procedure, i.e., electrospinning.

3.2.3. SEM analysis

The surface morphology, location of nanoparticles, and their effect on the nanofiber diameter and configuration were investigated by SEM analysis and are depicted in Fig. 4. It can be inferred that ECPNs have smooth and uniform surface morphology, with average diameter sizes smaller than 100 nm and without forming bead defects. Including nanoparticles into the nanofiber composites did not disturb the nanofiber integrity and surface morphology. The SEM images showed that the nanoparticles were fully embedded inside the nanofibers, likely due to their interactions with the CS/PVA matrix [16]. Furthermore, energy dispersive X-ray spectroscopy (EDS) images (Fig. S1) of ECPN/T@U nanofibers show that these samples are composed of carbon (70 %), oxygen (29 %), and zirconium (1 %) elements.

3.3. Dye adsorption experiments

3.3.1. Adsorption kinetics

Fig. 5 displays the removal efficiency of specimens toward cationic MB and anionic CR dyes. Nanoparticles exhibited fast adsorption kinetics (Fig. 5a, c) in the first ≈ 20 min, followed by a gradual improvement in removal performance and ultimately reaching equilibrium after 1 hour. Compared to nanoparticles, nanofiber composites feature a slower removal rate (Fig. 5 c, d).

The nanofiber composites demonstrated a fast kinetic stage at the beginning (60 min) followed by a slow phase, reaching equilibrium within 180 min. It can be inferred from Fig. 5a that ND showed the lowest adsorption removal toward cationic MB dye, while TOND showed the highest removal efficiency toward this dye. Possibly, this observation can be explained by the presence of more carboxylic acid

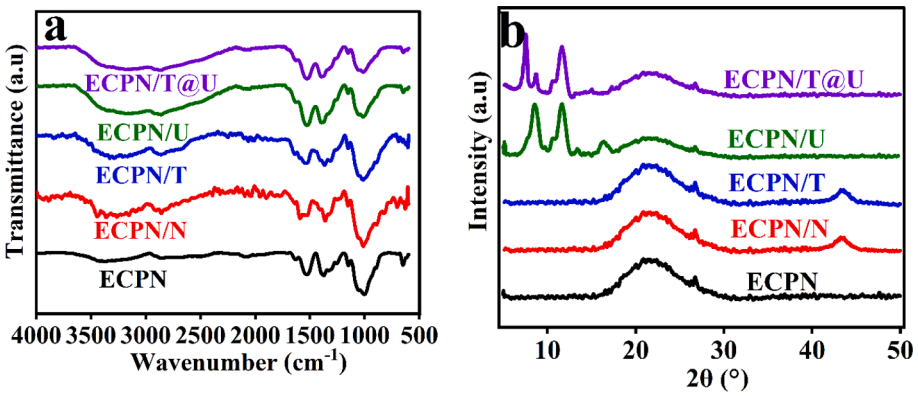

Fig. 3. a) FTIR spectra and b) XRD patterns of electrospun nanofibers holding 1.5 wt% of various nanoparticles.

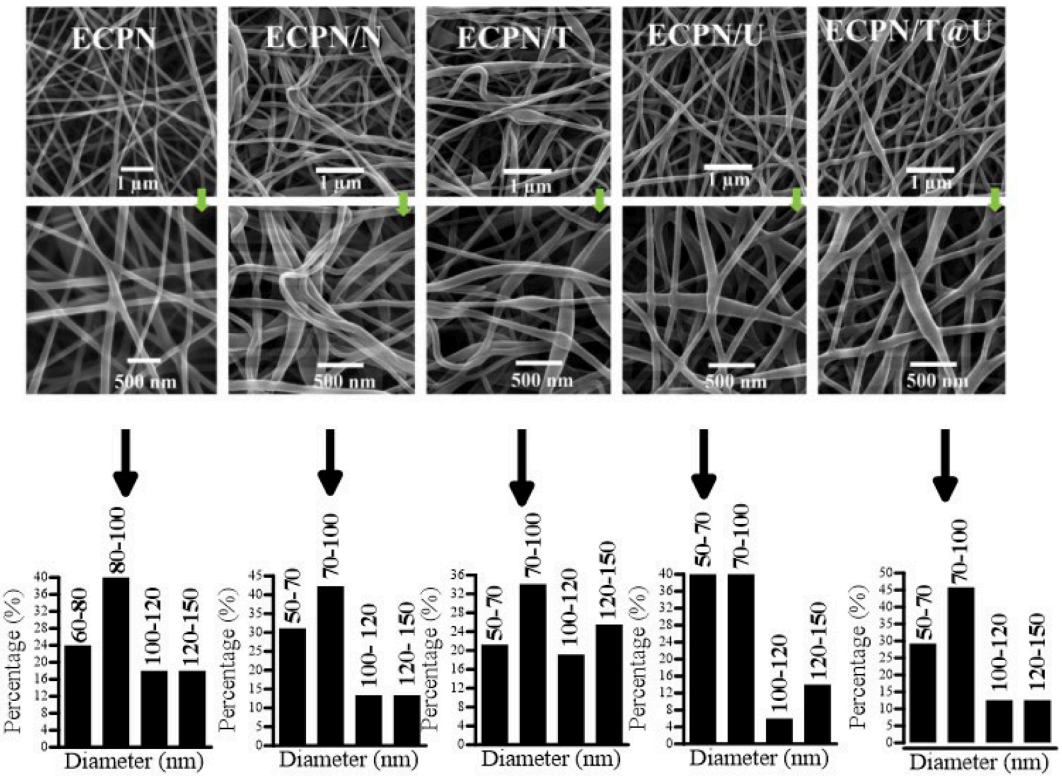

Fig. 4. SEM images of the fabricated electrospun nanofiber composites containing 1.5 wt% of different adsorbent nanoparticles.

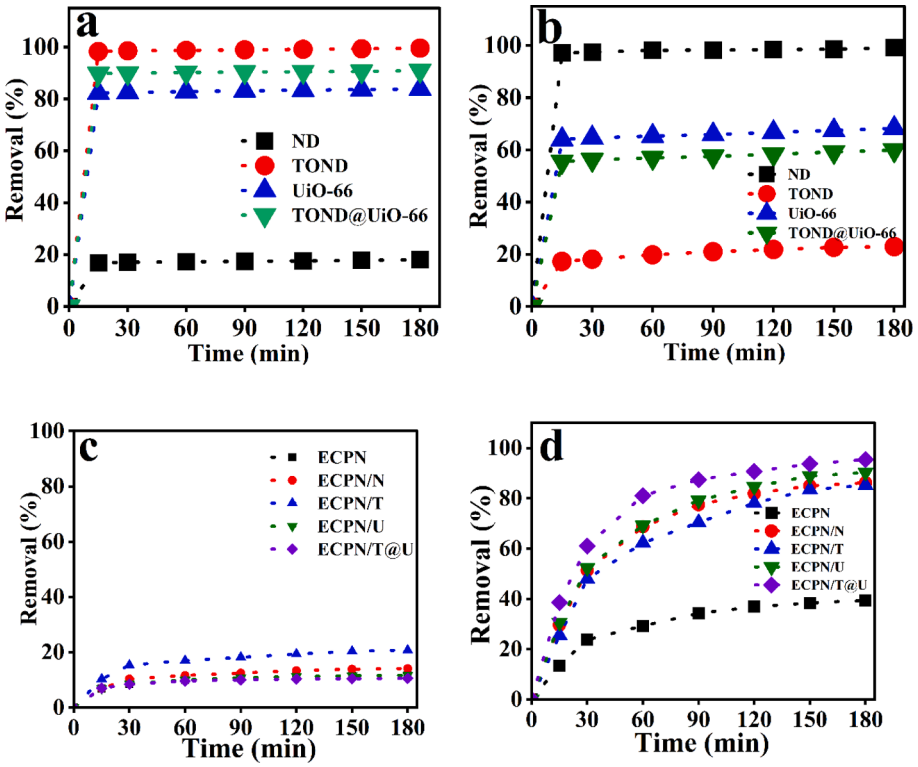

Fig. 5. Removal efficiency of the nanoparticles and their electrospun nanofibers composite toward a, c) MB and b, d) CR dyes.

functional groups and, consequently, more negative surface charges of TOND particles. That is, electrostatic attraction between cationic MB molecules and the negatively-charged TOND will increase, resulting in higher adsorption of MB [31,60].

As a result of the hybridization of UiO-66 with TOND, MB's removal efficiency increased, primarily due to enhancing the electrostatic attraction between adsorbate-adsorbents as a result of increasing the negative surface charge of UiO-66 nanoparticles (Table 2). Accordingly,

the removal efficiencies of the nanoparticles toward MB dye are in the following order: ND (18.0 %) < UiO-66 (83.8 %) < TOND@UiO-66 (90.9 %) < TOND (99.6 %). However, a completely different trend in the removal performance of nanoparticles toward CR was observed, as shown in Fig. 5b. Accordingly, ND showed the best performance by removing 99.1 % of anionic CR dye, followed by UiO-66 (68.3 %), TOND@UiO-66 (59.9 %), and TOND (22.9 %). This observation can be justified by the different charges of the dye and their chemical structure.

The BET surface area for ND is about 291 m^2/g (Table 2), which was not too large to account for the high removal performance toward anionic CR, so looking for other contributing factors is imperative. In addition, the negative surface charge of ND could trigger the charge repulsion between ND and CR molecules. It is, therefore, possible that other adsorption mechanisms, such as hydrogen bonding or hydrophobic-hydrophobic interactions, are involved. A comparison between the FTIR spectrum of adsorbents before and after adsorption could provide valuable insight into the adsorption mechanism. As depicted in Fig. S2, the intensities of absorption bands at 1541 and 1683 cm^{-1} increased after the adsorption of CR onto all adsorbent nanoparticles due to the presence of azo (–N═N–) groups in the structure of CR molecules. Two $–SO_3^-$ groups in the chemical structure of the CR molecule and their oxygen atoms could act as a hydrogen-bonding acceptor and create intramolecular hydrogen bonds with the polar groups of the adsorbent nanoparticles. As a result of this interaction, the positions of characteristic bands of this group (at 1401 and 11120 cm^{-1}) slightly shifted to the lower wavenumbers [40]. The formation of hydrogen bonds between CR molecules and the synthesized adsorbent nanoparticles was further confirmed by increasing the intensity of the broad absorption bands at 3150–3600 cm^{-1} due to the formation of hydrogen bonds between the $–NH_2$ and $–SO_3$ groups of CR molecules and the polar groups of the adsorbent nanoparticles. Other researchers also observed similar results when removing MO and acid orange 7 from water by ND [40] and modified CNTs [61].

For pure MB, characteristic absorption bands at about 1084, 1316, and 1586 can be ascribed to $–CH_3$, –C—N, and –C═S bonds, respectively. The FTIR spectrum of adsorbents showed a slight increase in the intensity of bands in the range of 2850–2950 cm^{-1} after the adsorption of MB, perhaps caused by stretching vibrations in –C—H bonds [37]. The aromatic rings in the structure of both dyes promise their π-π interaction with the π electron-rich regions of the nanoparticles, which can be further seen in the reduction of –C═C stretching vibration intensity of nanoparticles [61]. Hence, the nanoparticles are capable of adsorbing anionic CR molecules via hydrogen bonds and electrostatic interactions while adsorbing cationic MB molecules via π-π and electrostatic interactions.

Fig. 5c shows that all nanocomposite nanofibers had relatively low removal efficiencies for cationic MB dye, owing to the protonation of the CS/PVA matrix [59]. Accordingly, the removal efficiency of nanofibers toward cationic MB dye is in the order of ECPN/T@U (10.5 %) < ECPN (11.6 %) < ECPN/U (11.7 %) < ECPN/N (14.1 %) < ECPN/T (20.8 %), significantly lower than those observed for their parent nanoparticles (Fig. 5a). There is a possibility that the relatively higher removal efficiency of ECPN/T toward cationic MB dye might be due to the high negative charge of the TOND particles, which reduces the positive charge of the CS/PVA matrix.

As shown in Fig. 5d, adding different nanoparticles significantly improved the removal efficiency of pure nanofibers toward anionic CR dye. Therefore, the removal efficiencies of nanofibers towards anionic CR dye are as follows: ECPN (39.4 %) < ECPN/T (85.2 %) < ECPN/N (86.2 %) < ECPN/U (90.3 %) < ECPN/T@U (95.4 %). The enhancement in effective surface area and porosity of nanocomposite could be responsible for the latter observation. The electrostatic attraction allows CR to interact strongly with positively charged nanofibers. Therefore, electrostatic attraction and hydrogen bonding may be involved in the adsorption of anionic CR molecules by the nanofibers, as schematically illustrated in Scheme 2.

Adsorption of organic dyes on adsorbent materials is a physicochemical process that involves the transfer of the dissolved molecules from the aqueous phase to the surface of adsorbent materials. Consequently, three well-known kinetic models, including pseudo-first-order, pseudo-second-order, and intra-particle diffusion models, were employed to clarify the adsorption behavior of the synthesized adsorbent materials toward dyes [62,63]. Table 3 summarizes the determination coefficients (R^2) and kinetic parameters determined by fitting the experimental data to the above-stated kinetic models (Figs. S3 and S4).

The R^2 values from the pseudo-second-order kinetic model are greater than 0.99 for the adsorption of both organic dyes on the synthesized adsorbent materials. Moreover, all the calculated adsorption capacities ($q_{e,\ ca}$) are nearly close to those measured experimentally ($q_{e,\ exp}$). This suggests that MB and CR dye adsorption behavior over the synthesized adsorbent materials is better predicted with a pseudo-second-order kinetic model, implying that the rate-controlling step in this adsorption process might be chemisorption [62,64].

3.3.2. Adsorption isotherms

The data related to the adsorption performance of nanofibers for removing MB and CR at various initial dye concentrations (20–500 mg/L) are depicted in Fig. 6a and b, respectively. All nanofibers showed a sharp increase in adsorption capacity for removing MB before reaching equilibrium (Fig. 6a). Accordingly, the maximum equilibrium adsorption capacity of cationic MB dye over the nanofibers was as follows: ECPN (62 mg/g) < ECPN/U (212 mg/g) < ECPN/N (229 mg/g) < ECPN/T@U (244 mg/g) < ECPN/T (307 mg/g), indicating an approximately four-time increase in the adsorption capacity of ECPN after adding only 1.5 wt% of TOND.

Comparing Fig. 6a and b reveals that the maximum equilibrium adsorption capacities of anionic CR dye over nanofibers are much higher than those of cationic MB dye, possibly due to the prominent role of the dye removal mechanism by electrostatic interactions. Accordingly, the maximum equilibrium adsorption capacity of anionic CR dye over the fabricated nanofibers increased in the order of ECPN (644 mg/g) < ECPN/T (719 mg/g) < ECPN/N (722 mg/g) < ECPN/U (733 mg/g) < ECPN/T@U (1085 mg/g), indicating approximately 68 % improvement in the adsorption performance of ECPN/T@U in comparison with ECPN.

Four well-known isotherms, including Langmuir, Freundlich, Dubinin-Radushkevich, and Tempkin isotherms, were employed to get further insight into the interaction of dye molecules with nanofiber adsorption active sites. The associated data compiled in Fig. S5 (Supplementary Information file) and Table 4 demonstrates that R^2 values belonging to the Langmuir isotherm model for removing CR are among the highest values (ranging from 0.990 to 0.998), suggesting monolayer adsorption of CR molecules onto the homogeneous surface of the nanocomposite nanofibers.

The higher R^2 values of the Tempkin isotherm model for eliminating MB and the corresponding n_F values higher than one suggest the favorable nature of the adsorption processes [58]. Moreover, the mean energy values for both organic dyes calculated by the Dubinin-Radushkevich isotherm model are below 5000 J/mol, indicating that physical adsorption dominates the adsorption mechanism of both organic dyes onto the fabricated nanofibers [61]. The maximum adsorption capacity of ECPN/T@U obtained from the Langmuir model towards CR was compared with those in the literature (Table S1). It is inferred that the maximum adsorption capacity of ECPN/T@U (1428.68 mg/g) surpasses most reported adsorbents in the literature. In addition, as illustrated in Fig. S6, ECPN/T@U showed appreciable selectivity toward anionic CR dye in the CR/MB mixture. Consequently, the designed nanofiber composite appears to be an excellent candidate for effectively and selectively removing the anionic organic dyes.

3.3.3. Thermodynamics of adsorption

To better understand the adsorption process of CR and MB dyes, the effect of temperature on the adsorption performance of ECPN/T@U

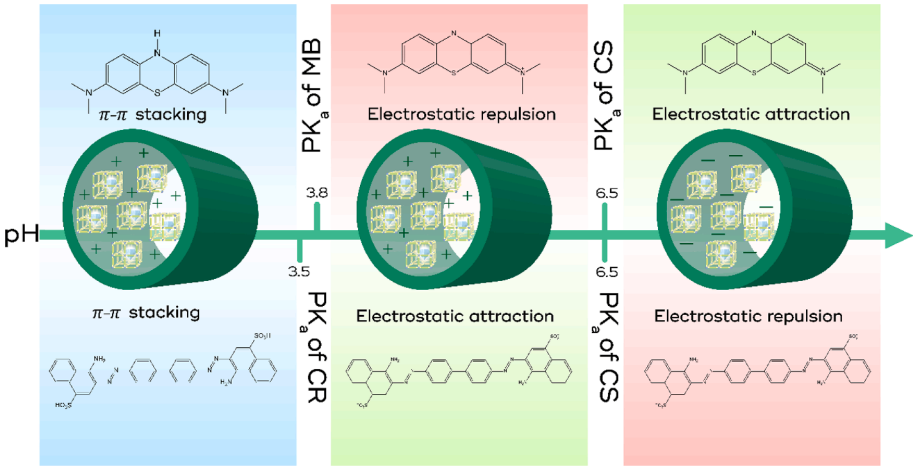

Scheme 2. Plausible adsorption mechanisms as a function of pH.

Table 3
Kinetic parameters for removing MB and CR dyes by the synthesized adsorbent materials.

Adsorbents	Dyes	R^2			q_e (mg/g)		K_2 (g/mg*min)
		Pseudo-first order	Pseudo-second order	Intraparticle diffusion	Calculated	Experimental	
ND	MB	0.973	0.999	0.971	18.18	18.01	2.4×10^{-2}
	CR	0.950	0.999	0.953	99.01	99.12	1.8×10^{-2}
TOND	MB	0.948	0.999	0.981	100.00	99.56	2.3×10^{-2}
	CR	0.928	0.998	0.993	23.86	22.92	4.3×10^{-3}
UiO-66	MB	0.964	0.999	0.996	84.03	83.82	1.9×10^{-2}
	CR	0.949	0.999	0.974	68.49	68.27	6.3×10^{-3}
TOND@UiO-66	MB	0.995	0.999	0.997	90.91	90.93	2.7×10^{-2}
	CR	0.926	0.999	0.978	60.24	59.89	6.1×10^{-3}
Nanofiber composite							
ECPN	MB	0.972	0.999	0.929	12.50	11.62	5.8×10^{-3}
	CR	0.979	0.998	0.928	41.16	39.43	6.2×10^{-4}
ECPN/N	MB	0.948	0.998	0.901	15.48	14.11	3.5×10^{-3}
	CR	0.983	0.997	0.902	89.09	86.19	3.0×10^{-4}
ECPN/T	MB	0.963	0.998	0.901	22.62	20.76	2.4×10^{-3}
	CR	0.970	0.996	0.941	87.26	85.19	2.2×10^{-4}
ECPN/U	MB	0.982	0.999	0.931	12.53	11.66	5.8×10^{-3}
	CR	0.983	0.998	0.925	92.69	90.31	2.6×10^{-4}
ECPN/T@U	MB	0.987	0.999	0.878	11.04	10.52	1.0×10^{-2}
	CR	0.993	0.998	0.874	99.69	95.42	3.9×10^{-4}

toward both CR and MB dyes was investigated by changing the adsorption temperature from 25 to 45 °C (details are summarized in the Supplementary Information). It can be observed from Table S2 that by increasing the temperature, the adsorption capacities of both anionic and cationic dyes onto the ECPN/T@U decreased, indicating the exothermic nature of this adsorption process. Moreover, the negative values of ΔH^0 further confirmed that the adsorption process is exothermic. The negative values of ΔG^0 indicated that the adsorption of these dyes onto the ECPN/T@U is a spontaneous process [65]. However, the negative values of ΔS^0 are unfavorable for spontaneous adsorption, demonstrating that the system's randomness decreases during the adsorption of these dyes.

3.3.4. *Effect of ionic strength and pH*

In industrial wastewater, several interfering agents, such as surfactants, salts, heavy metal ions, etc., can affect the adsorption process [66]; for instance, in its simplest form, by altering the ionic strength of the medium [67]. According to two opposite mechanisms, ionic strength can either accelerate or decelerate dye removal, including i) facilitating dye dissociation, which results in an improvement in dye removal efficiency, and ii) reducing the electrostatic attraction between dye molecules and adsorbent particles [35,60]. Therefore, the effect of ionic strength on the removal efficiency of ECPN/T@U toward MB and CR dyes was investigated by adding different amounts of NaCl into the dye solutions. Fig. 6c displays the removal efficiency at three different concentrations of NaCl. Accordingly, the MB removal efficiency increased by increasing the NaCl concentration to the maximum removal efficiency of 26.3 % at a concentration of 0.5 mol/L. This observation might be due to MB molecule dissociation, which may enhance the dye removal efficiency of ECPN/T@U. However, it was found that adding NaCl into the CR solution reduced CR removal efficiency, mainly because of the screening of electrostatic interactions between anionic CR molecules and positively-charged surfaces of ECPN/T@U.

The effect of pH was also investigated on the removal efficiency of ECPN/T@U. The pH of the dye solution can affect the adsorption performance by protonation and deprotonation of the CS/PVA matrix [35]. It was reported that acidic solutions are more favorable for removing anionic dyes by pure CS adsorbent compared to basic solutions. However, the cross-linked CS/PVA showed good stability against highly acidic and basic solutions. Accordingly, this study explored the adsorption performance in a wide range of pH, from 3 to 13.

Fig. 6d displays the removal efficiency of ECPN/T@U toward MB and CR dyes as a function of solution pH. As shown in Fig. 6d, the removal efficiency of cationic MB decreased by increasing pH from 3.2 to 6.2 and then increased continuously with a further increment of pH from 6.2 to

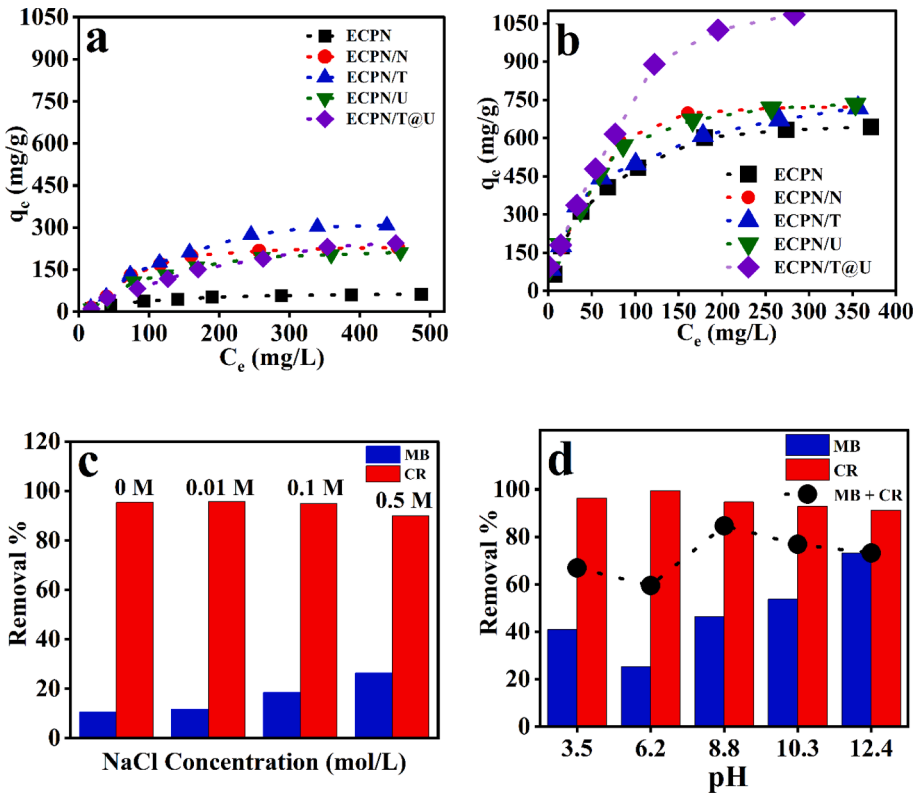

Fig. 6. Adsorption isotherms of electrospun nanofiber composites for removing a) MB and b) CR dyes; effects of c) NaCl concentration and d) pH on the removal efficiency of ECPN/T@U toward MB and CR dyes.

Table 4
Isotherm parameters for the adsorption of MB and CR onto the fabricated nanofiber composites.

Nanofiber composites		ECPN		ECPN/N		ECPN/T		ECPN/U		ECPN/T@U	
Dyes		MB	CR	MB	CR	MB	CR	MB	CR	MB	CR
Langmuir	q_{max} (mg/g)	75.75	769.23	384.61	833.34	500.0	791.54	416.66	873.66	714.28	1428.68
	K_L (L/mg)	0.0103	0.0172	0.0042	0.0233	0.0028	0.0226	0.0028	0.0244	0.0013	0.0127
	R^2	0.998	0.996	0.692	0.988	0.910	0.993	0.614	0.990	0.371	0.991
Freundlich	K_F (mg/g)	3.23	34.53	2.46	56.38	1.65	57.47	1.62	67.92	1.18	78.61
	n	1.97	1.85	1.23	2.11	1.08	2.20	1.16	2.30	1.09	2.15
	R^2	0.950	0.912	0.853	0.952	0.911	0.972	0.893	0.970	0.935	0.944
Dubinin-Radushkevich	q_{max} (mg/g)	48.84	475.23	181.90	481.16	211.98	462.89	154.34	478.95	153.45	564.25
	B	8.0×10^{-5}	2.0×10^{-5}	1.0×10^{-4}	3.0×10^{-6}	1.0×10^{-4}	3.0×10^{-6}	1.0×10^{-4}	2.0×10^{-6}	2.0×10^{-4}	5.0×10^{-7}
	E (J/mol)	790	1500	70	400	70	400	70	500	50	1000
	R^2	0.807	0.852	0.894	0.624	0.861	0.673	0.874	0.624	0.862	0.521
Tempkin	B_T (KJ/mol)	152.20	16.13	34.59	16.33	24.91	17.65	37.26	17.75	33.04	13.44
	A_T (L/g)	0.108	0.217	0.072	0.388	0.054	0.396	0.060	0.525	0.04	0.565
	R^2	0.990	0.991	0.957	0.924	0.983	0.970	0.984	0.928	0.962	0.786

12.4. At low pH values (lower than the pKa value of MB ≈ 3.8 [64]), MB molecules are in neutral form and unable to interact via electrostatic interactions with the positively-charged surface of adsorbent materials. As an ideal planar molecule, MB can interact with an adsorbent material's electron-rich regions [61]. Therefore, π-π stacking interactions between MB molecules and ECPN/T@U at low pH could be responsible for the removal of the MB, schematically illustrated in Scheme 2. In light of CS's pKa of approximately 6.5, it exists in a protonated state in acidic media and deprotonated in the basic environment. Thus, in the pH range of 3.8–6.5, both MB molecules and ECPN/T@U carry positive charges. Hence, increasing the pH enhances the repulsion between adsorbate and adsorbent and will reduce the ECPN/T@U efficiency for cationic MB dye removal.

Further enhancement of pH will increase the negative charges on both TOND@UiO-66 and CS/PVA, which is desirable for removing MB via strong electrostatic attractions. ECPN/T@U exhibited a maximum removal efficiency of 99.5 % for anionic CR dye at pH 6.2, which is similar to the results obtained with CS and its derivatives for adsorptive dye removal [35,59]. However, as mentioned above, increasing pH will induce a more negative charge on the surface of ECPN/T@U and impede the adsorption of anionic CR molecules due to the creation of electrostatic repulsion between adsorbate-adsorbent. As a result, the removal efficiency of ECPN/T@U toward anionic CR dye constantly decreased with increasing the solution pH from 6.2 to 12.4.

3.3.5. Adsorption mechanism

Plausible removal mechanisms for ECPN/T@U, according to our tests on the effect of ionic strength, pH, and FTIR spectra of the adsorbents before and after adsorption, are illustrated in Scheme 2. Accordingly, ECPN/T@U is proposed to interact with cationic MB molecules via π-π stacking interactions (pH < 3.8), electrostatic repulsion (3.8 < pH < 6.5), and electrostatic attraction (6.5 < pH). Concerning the interactions with anionic CR molecules, one expects π-π stacking interactions (pH < 3.5), electrostatic attraction and hydrogen bonding (3.5 < pH < 6.5), and electrostatic repulsion (6.5 < pH).

3.3.6. Reusability of ECPN/T@U for dye removal

The reusability of ECPN/T@U was evaluated by investigating the removal efficiency of the regenerated nanofibers over repeated adsorption–desorption cycles. Desorption and regeneration of CR-loaded ECPN/T@U were achieved by washing the spent adsorbent with an alkaline ethanol solution (containing 0.5 % NaOH), whereas the MB-loaded ECPN/T@U adsorbent was washed with an acidic ethanol solution (containing 0.5 % HCl) [59]. Accordingly, after each adsorption cycle, the dye-loaded ECPN/T@U was washed with water and alkaline or acidic ethanol solution to desorb the dye molecules entirely. Then, the regenerated ECPN/T@U was dried at 60 °C under vacuum for 12 h. It can be seen from Fig. 7 that the removal efficiency of ECPN/T@U toward both anionic and cationic dyes slightly decreased with increasing the number of adsorption–desorption cycles. The acceptable reusability of the spent ECPN/T@U and its relatively high removal efficiency of 90.1 % toward CR dye after 6 adsorption–desorption cycles demonstrate the potential of these adsorbent materials for removing anionic CR dye from wastewater.

4. Conclusion

We demonstrated a facile electrospinning method to prepare rationally desinged (UiO-66 MOFs)-loaded chitosan/polyvinyl alcohol (PVA) nanofibers for dye-contaminated water treatment. According to the prominent role of polymeric substrate in the adsorption performance of MOF nanofibers, chitosan, a functional biobased polymer with abundant amino and hydroxyl functional groups, was added to polyvinyl alcohol to incorporate active functional groups for better dye removal. The unique features of MOF-based polymeric nanofibers, such as ease of handling, straightforward separation from treated water, and regeneration ability, make them appealing compared to pure MOF powder for real-world applications. Moreover, a hybridization approach was developed by binding thermally oxidized nanodiamond (TOND) with UiO-66, named TOND@UiO-66, while keeping an eye on the final morphology and textural properties of nanofiber composites. The post-treatment, i.e., chemical crosslinking of the nanofibers with glutaraldehyde, made the substrate structurally stable for water treatment. Our results show that incorporating 1.5 wt% of TOND@UiO-66 into the pure polymeric nanofiber doubled the maximum Langmuir adsorption capacity of anionic Congo red, from 770 to 1430 mg/g. We also clarified different mechanisms responsible for removing cationic and anionic dyes from aqueous solutions at various pH and in the presence of given counter-ions. Multiple interactions between dyes and the designed adsorbents, including π-π stacking and electrostatic interactions, as well as hydrogen bonding, can develop depending on the media's pH. As a critical factor in applications, the regeneration of adsorbents showed that the designed MOF-based nanofiber composites could survive repeated adsorption–desorption cycles (just a 10 % drop in performance after 6 cycles). Given the unique feature of the MOFs and the electrospinning approach, we believe that this combination will definitely spur the growth of the nascent area of MOF polymer nanocomposites for water remediation.

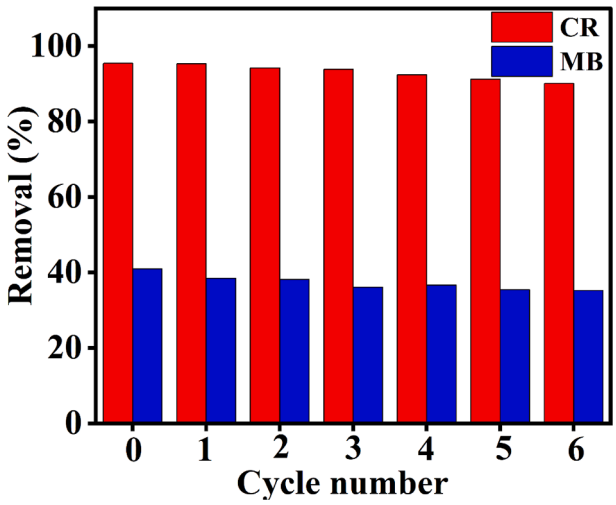

Fig. 7. Cyclic usage of ECPN/T@U for removing CR and MB dyes.

Declaration of Competing Interest

The authors declare that they have no known competing financial interests or personal relationships that could have appeared to influence the work reported in this paper.

Data availability

No data was used for the research described in the article.

Acknowledgment

Dr. Arjmand would like to thank the Canada Research Chairs program for the financial support. The authors would like to acknowledge Syilx Okanagan First Nation for allowing us to conduct research in their unceded ancestorial traditional territory. Mr. Ahmadijokani, Dr. Kamkar, and Dr. Rojas are grateful for funding support from the Canada Excellence Research Chair Program (CERC-2018-00006) and the Canada Foundation for Innovation (Project number 38623). Dr. Rojas also acknowledges the European Research Council under the European Union's Horizon 2020 research and innovation program (ERC Advanced grant No. 788489, "BioElCell"). The authors also would like to thank Mr. Aydin Badrian (aydinbadrian.com) for his efforts on the graphical parts of this study.

Appendix A. Supplementary data

Supplementary data to this article can be found online at https://doi.org/10.1016/j.cej.2022.141176.

References

[1] S. Rojas, P. Horcajada, Metal–organic frameworks for the removal of emerging organic contaminants in water, Chem. Rev. 120 (16) (2020) 8378–8415.
[2] F. Ahmadijokani, H. Molavi, M. Rezakazemi, T.M. Aminabhavi, M. Arjmand, Simultaneous detection and removal of fluoride from water using smart metal-organic framework-based adsorbents, Coord. Chem. Rev. 445 (2021), 214037.
[3] F. Ahmadijokani, H. Molavi, M. Rezakazemi, S. Tajahmadi, A. Bahi, F. Ko, T. M. Aminabhavi, J.-R. Li, M. Arjmand, UiO-66 metal-organic frameworks in water treatment: A critical review, Prog. Mater Sci. 100904 (2021).
[4] F. Ahmadijokani, H. Molavi, S. Tajahmadi, M. Rezakazemi, M. Amini, M. Kamkar, O.J. Rojas, M. Arjmand, Coordination chemistry of metal–organic frameworks: Detection, adsorption, and photodegradation of tetracycline antibiotics and beyond, Coord. Chem. Rev. 464 (2022), 214562.
[5] H. Molavi, H. Moghimi, R.A. Taheri, Zr-based MOFs with high drug loading for adsorption removal of anti-cancer drugs: a potential drug storage, Appl. Organomet. Chem. 34 (4) (2020) e5549.

[6] R.J. Drout, L. Robison, S. Hanna, O.K. Farha, Can Metal-Organic Framework Composites Contain the Water Contamination Crisis?<? ACS-CT-END-Insert?>, ACS Publications, 2018.

[7] M. Mon, R. Bruno, J. Ferrando-Soria, D. Armentano, E. Pardo, Metal–organic framework technologies for water remediation: towards a sustainable ecosystem, J. Mater. Chem. A 6 (12) (2018) 4912–4947.

[8] A. Ejsmont, J. Andreo, A. Lanza, A. Galarda, L. Macreadie, S. Wuttke, S. Canossa, E. Ploetz, J. Goscianska, Applications of reticular diversity in metal–organic frameworks: An ever-evolving state of the art, Coord. Chem. Rev. 430 (2021), 213655.

[9] N. Anahidzade, A. Abdolmaleki, M. Dinari, K.F. Tadavani, M. Zhiani, Metal-organic framework anchored sulfonated poly (ether sulfone) as a high temperature proton exchange membrane for fuel cells, J. Membr. Sci. 565 (2018) 281–292.

[10] U. Ryu, S. Jee, P.C. Rao, J. Shin, C. Ko, M. Yoon, K.S. Park, K.M. Choi, Recent advances in process engineering and upcoming applications of metal–organic frameworks, Coord. Chem. Rev. 426 (2021), 213544.

[11] R. Freund, O. Zaremba, G. Arnauts, R. Ameloot, G. Skorupskii, M. Dincă, A. Bavykina, J. Gascon, A. Ejsmont, J. Goscianska, The current status of MOF and COF applications, Angew. Chem. Int. Ed. 60 (45) (2021) 23975–24001.

[12] F. Haase, P. Hirschle, R. Freund, S. Furukawa, Z. Ji, S. Wuttke, Beyond Frameworks: Structuring Reticular Materials across Nano-, Meso-, and Bulk Regimes, Angew. Chem. Int. Ed. 59 (50) (2020) 22350–22370.

[13] Z. Ji, R. Freund, C.S. Diercks, P. Hirschle, O.M. Yaghi, S. Wuttke, From Molecules to Frameworks to Superframework Crystals, Adv. Mater. 33 (42) (2021) 2103808.

[14] A.G. Slater, A.I. Cooper, Function-led design of new porous materials, Science 348 (6238) (2015) aaa8075.

[15] F. Ahmadijokani, H. Molavi, A. Bahi, R. Fernández, P. Alaee, S. Wu, S. Wuttke, F. Ko, M. Arjmand, Metal-Organic Frameworks and Electrospinning: A Happy Marriage for Wastewater Treatment, Adv. Funct. Mater. 2207723 (2022).

[16] G.W. Peterson, D.T. Lee, H.F. Barton, T.H. Epps, G.N. Parsons, Fibre-based composites from the integration of metal–organic frameworks and polymers, Nat. Rev. Mater. 6 (7) (2021) 605–621.

[17] A.M. Al-Dhahebi, J. Ling, S.G. Krishnan, M. Yousefzadeh, N.K. Elumalai, M.S. M. Saheed, S. Ramakrishna, R. Jose, Electrospinning research and products: The road and the way forward, Appl. Phys. Rev. 9 (1) (2022), 011319.

[18] X. Fan, L. Yu, L. Li, C. Yang, J. Wen, X. Ye, J. Cheng, Y. Hu, Characterization and application of zeolitic imidazolate framework-8@ polyvinyl alcohol nanofibers mats prepared by electrospinning, Mater. Res. Express 4 (2) (2017), 026404.

[19] L. Jin, J. Ye, Y. Wang, X. Qian, M. Dong, Electrospinning synthesis of ZIF-67/PAN fibrous membrane with high-capacity adsorption for malachite green, Fibers Polym. 20 (10) (2019) 2070–2077.

[20] I. Ahmed, S.H. Jhung, Composites of metal–organic frameworks: preparation and application in adsorption, Mater. Today 17 (3) (2014) 136–146.

[21] A. Valverde, D. Payno, L. Lezama, J.M. Laza, S. Wuttke, R. Fernández de Luis, Multivariate Functionalization of UiO-66 for Photocatalytic Water Remediation, Adv. Sustain. Syst. (2022) 2200024.

[22] R. Ettlinger, U. Lächelt, R. Gref, P. Horcajada, T. Lammers, C. Serre, P. Couvreur, R. E. Morris, S. Wuttke, Toxicity of metal–organic framework nanoparticles: from essential analyses to potential applications, Chem. Soc. Rev. (2022).

[23] S. Canossa, S. Wuttke, Functionalization chemistry of porous materials, 2020, p. 2003875.

[24] J. Abdi, M. Vossoughi, N.M. Mahmoodi, I. Alemzadeh, Synthesis of metal-organic framework hybrid nanocomposites based on GO and CNT with high adsorption capacity for dye removal, Chem. Eng. J. 326 (2017) 1145–1158.

[25] J. Abdi, F. Banisharif, A. Khataee, Amine-functionalized Zr-MOF/CNTs nanocomposite as an efficient and reusable photocatalyst for removing organic contaminants, J. Mol. Liq. 334 (2021), 116129.

[26] M. Neshastehgar, P. Rahmani, A. Shojaei, H. Molavi, Enhanced adsorption removal performance of UiO-66 by rational hybridization with nanodiamond, Micropor. Mesopor. Mater. 296 (2020), 110008.

[27] S. Ahmadipouya, M.H. Haris, F. Ahmadijokani, A. Jarahiyan, H. Molavi, F. M. Moghaddam, M. Rezakazemi, M. Arjmand, Magnetic Fe3O4@ UiO-66 nanocomposite for rapid adsorption of organic dyes from aqueous solution, J. Mol. Liq. 322 (2021), 114910.

[28] M. Dinari, F. Jamshidian, Preparation of MIL-101-NH2 MOF/triazine based covalent organic framework hybrid and its application in acid blue 9 removals, Polymer 215 (2021), 123383.

[29] K.L.B. Solis, Y.-H. Kwon, M.-H. Kim, H.-R. An, C. Jeon, Y. Hong, Metal organic framework UiO-66 and activated carbon composite sorbent for the concurrent adsorption of cationic and anionic metals, Chemosphere 238 (2020), 124656.

[30] S. Mallakpour, E. Azadi, M. Dinari, Removal of cationic and anionic dyes using Ca-alginate and ZnAl layered double hydroxide/metal-organic framework, Carbohydr. Polym. 120362 (2022).

[31] H. Molavi, A. Shojaei, A. Pourghaderi, Rapid and tunable selective adsorption of dyes using thermally oxidized nanodiamond, J. Colloid Interface Sci. 524 (2018) 52–64.

[32] M. Zamani, M. Aghajanzadeh, H. Molavi, H. Danafar, A. Shojaei, Thermally oxidized nanodiamond: an effective sorbent for separation of methotrexate from aqueous media: synthesis, characterization, in vivo and in vitro biocompatibility study, J. Inorg. Organomet. Polym Mater. 29 (3) (2019) 701–709.

[33] F. Ahmadijokani, H. Molavi, A. Peyghambari, A. Shojaei, M. Rezakazemi, T. M. Aminabhavi, M. Arjmand, Efficient removal of heavy metal ions from aqueous media by unmodified and modified nanodiamonds, J. Environ. Manage. 316 (2022), 115214.

[34] P. Karami, S.S. Khasraghi, M. Hashemi, S. Rabiei, A. Shojaei, Polymer/nanodiamond composites-a comprehensive review from synthesis and fabrication to properties and applications, Adv. Colloid Interface Sci. 269 (2019) 122–151.

[35] M. Raeiszadeh, A. Hakimian, A. Shojaei, H. Molavi, Nanodiamond-filled chitosan as an efficient adsorbent for anionic dye removal from aqueous solutions, J. Environ. Chem. Eng. 6 (2) (2018) 3283–3294.

[36] K. Mirzaei, E. Jafarpour, A. Shojaei, H. Molavi, Facile Synthesis of Polyaniline@ UiO-66 Nanohybrids for Efficient and Rapid Adsorption of Methyl Orange from Aqueous Media, Ind. Eng. Chem. Res. (2022).

[37] H. Molavi, M. Neshastehgar, A. Shojaei, H. Ghashghaeinejad, Ultrafast and simultaneous removal of anionic and cationic dyes by nanodiamond/UiO-66 hybrid nanocomposite, Chemosphere 247 (2020), 125882.

[38] D.V. Mousavi, S. Ahmadipouya, A. Shokrgozar, H. Molavi, M. Rezakazemi, F. Ahmadijokani, M. Arjmand, Adsorption performance of UiO-66 towards organic dyes: Effect of activation conditions, J. Mol. Liq. 321 (2021), 114487.

[39] Z. Delavar, A. Shojaei, Enhanced mechanical properties of chitosan/nanodiamond composites by improving interphase using thermal oxidation of nanodiamond, Carbohydr. Polym. 167 (2017) 219–228.

[40] H.-D. Wang, Q. Yang, C.H. Niu, I. Badea, Adsorption of azo dye onto nanodiamond surface, Diam. Relat. Mater. 26 (2012) 1–6.

[41] A. Mohammadi, A. Shojaei, S.S. Khasraghi, A.K. Ghavidel, Synthesis of high-reinforcing-silica@ nanodiamond nanohybrids as efficient particles for enhancement of mechanical, thermal, and rolling resistance of styrene-butadiene rubber, Polymer 255 (2022), 125122.

[42] W. Xu, M. Dong, L. Di, X. Zhang, A facile method for preparing UiO-66 encapsulated Ru catalyst and its application in plasma-assisted CO2 methanation, Nanomaterials 9 (10) (2019) 1432.

[43] X. Zhang, Y. Zhang, T. Wang, Z. Fan, G. Zhang, A thin film nanocomposite membrane with pre-immobilized UiO-66-NH 2 toward enhanced nanofiltration performance, RSC Adv. 9 (43) (2019) 24802–24810.

[44] M.A. Rodrigues, J. de Souza Ribeiro, E. de Souza Costa, J.L. de Miranda, H. C. Ferraz, Nanostructured membranes containing UiO-66 (Zr) and MIL-101 (Cr) for O2/N2 and CO2/N2 separation, Sep. Purif. Technol. 192 (2018) 491–500.

[45] X. Jiang, S. Li, S. He, Y. Bai, L. Shao, Interface manipulation of CO 2–philic composite membranes containing designed UiO-66 derivatives towards highly efficient CO 2 capture, J. Mater. Chem. A 6 (31) (2018) 15064–15073.

[46] T. Han, Y. Xiao, M. Tong, H. Huang, D. Liu, L. Wang, C. Zhong, Synthesis of CNT@ MIL-68 (Al) composites with improved adsorption capacity for phenol in aqueous solution, Chem. Eng. J. 275 (2015) 134–141.

[47] S.S. Khasraghi, A. Shojaei, U. Sundararaj, Highly biocompatible multifunctional hybrid nanoparticles based on Fe3O4 decorated nanodiamond with superior superparamagnetic behaviors and photoluminescent properties, Mater. Sci. Eng. C 114 (2020), 110993.

[48] P. Hu, Z. Zhao, X. Sun, Y. Muhammad, J. Li, S. Chen, C. Pang, T. Liao, Z. Zhao, Construction of crystal defect sites in N-coordinated UiO-66 via mechanochemical in-situ N-doping strategy for highly selective adsorption of cationic dyes, Chem. Eng. J. 356 (2019) 329–340.

[49] P. Rahmani, A. Shojaei, N.P. Tavandashti, Nanodiamond loaded with corrosion inhibitor as efficient nanocarrier to improve anticorrosion behavior of epoxy coating, J. Ind. Eng. Chem. 83 (2020) 153–163.

[50] B.J. Etzold, I. Neitzel, M. Kett, F. Strobl, V.N. Mochalin, Y. Gogotsi, Layer-by-layer oxidation for decreasing the size of detonation nanodiamond, Chem. Mater. 26 (11) (2014) 3479–3484.

[51] S. Zhao, D. Chen, F. Wei, N. Chen, Z. Liang, Y. Luo, Removal of Congo red dye from aqueous solution with nickel-based metal-organic framework/graphene oxide composites prepared by ultrasonic wave-assisted ball milling, Ultrason. Sonochem. 39 (2017) 845–852.

[52] X. Sun, Q. Xia, Z. Zhao, Y. Li, Z. Li, Synthesis and adsorption performance of MIL-101 (Cr)/graphite oxide composites with high capacities of n-hexane, Chem. Eng. J. 239 (2014) 226–232.

[53] Y. Cao, Y. Zhao, Z. Lv, F. Song, Q. Zhong, Preparation and enhanced CO2 adsorption capacity of UiO-66/graphene oxide composites, J. Ind. Eng. Chem. 27 (2015) 102–107.

[54] F. Ahmadijokani, R. Mohammadkhani, S. Ahmadipouya, A. Shokrgozar, M. Rezakazemi, H. Molavi, T.M. Aminabhavi, M. Arjmand, Superior chemical stability of UiO-66 metal-organic frameworks (MOFs) for selective dye adsorption, Chem. Eng. J. 399 (2020), 125346.

[55] M.A. Abureesh, A.A. Oladipo, M. Gazi, Facile synthesis of glucose-sensitive chitosan–poly (vinyl alcohol) hydrogel: Drug release optimization and swelling properties, Int. J. Biol. Macromol. 90 (2016) 75–80.

[56] T. Jamnongkan, A. Wattanakornsiri, P.P. Pansila, C. Migliaresi, S. Kaewpirom, Effect of poly (vinyl alcohol)/chitosan ratio on electrospun-nanofiber morphologies, Advanced Materials Research, Trans Tech Publ, 2012, pp. 734–738.

[57] U.K. Parida, A.K. Nayak, B.K. Binhani, P. Nayak, Synthesis and characterization of chitosan-polyvinyl alcohol blended with cloisite 30B for controlled release of the anticancer drug curcumin, J. Biomater. Nanobiotechnol. 2 (04) (2011) 414.

[58] N.M. Mahmoodi, M. Oveisi, A. Taghizadeh, M. Taghizadeh, Synthesis of pearl necklace-like ZIF-8@ chitosan/PVA nanofiber with synergistic effect for recycling aqueous dye removal, Carbohydr. Polym. 227 (2020), 115364.

[59] A. Bayat, A. Tati, S. Ahmadipouya, S.A. Haddadi, M. Arjmand, Electrospun chitosan/polyvinyl alcohol nanocomposite holding polyaniline/silica hybrid nanostructures: an efficient adsorbent of dye from aqueous solutions, J. Mol. Liq. 331 (2021), 115734.

[60] H. Molavi, A. Pourghaderi, A. Shojaei, Experimental study on the influence of initial pH, ionic strength, and temperature on the selective adsorption of dyes onto nanodiamonds, J. Chem. Eng. Data 64 (4) (2019) 1508–1514.

[61] J. Ma, F. Yu, L. Zhou, L. Jin, M. Yang, J. Luan, Y. Tang, H. Fan, Z. Yuan, J. Chen, Enhanced adsorptive removal of methyl orange and methylene blue from aqueous solution by alkali-activated multiwalled carbon nanotubes, ACS Appl. Mater. Interfaces 4 (11) (2012) 5749–5760.
[62] J.-J. Li, C.-C. Wang, H.-F. Fu, J.-R. Cui, P. Xu, J. Guo, J.-R. Li, High-performance adsorption and separation of anionic dyes in water using a chemically stable graphene-like metal–organic framework, Dalton Trans. 46 (31) (2017) 10197–10201.
[63] J. Imanipoor, M. Mohammadi, M. Dinari, M.R. Ehsani, Adsorption and desorption of amoxicillin antibiotic from water matrices using an effective and recyclable MIL-53 (Al) metal–organic framework adsorbent, J. Chem. Eng. Data 66 (1) (2020) 389–403.
[64] H. Molavi, A. Hakimian, A. Shojaei, M. Raeiszadeh, Selective dye adsorption by highly water stable metal-organic framework: Long term stability analysis in aqueous media, Appl. Surf. Sci. 445 (2018) 424–436.
[65] M. Barjasteh, M. Vossoughi, M. Bagherzadeh, K.P. Bagheri, MIL-100 (Fe) a potent adsorbent of Dacarbazine: Experimental and molecular docking simulation, Chem. Eng. J. 452 (2023), 138987.
[66] F. Ahmadijokani, S. Tajahmadi, A. Bahi, H. Molavi, M. Rezakazemi, F. Ko, T. M. Aminabhavi, M. Arjmand, Ethylenediamine-functionalized Zr-based MOF for efficient removal of heavy metal ions from water, Chemosphere 264 (2021), 128466.
[67] K.-Y.A. Lin, H.-A. Chang, Ultra-high adsorption capacity of zeolitic imidazole framework-67 (ZIF-67) for removal of malachite green from water, Chemosphere 139 (2015) 624-631.